iScience

Article

Nuclear talin-1 provides a bridge between cell adhesion and gene expression

Graphical abstract

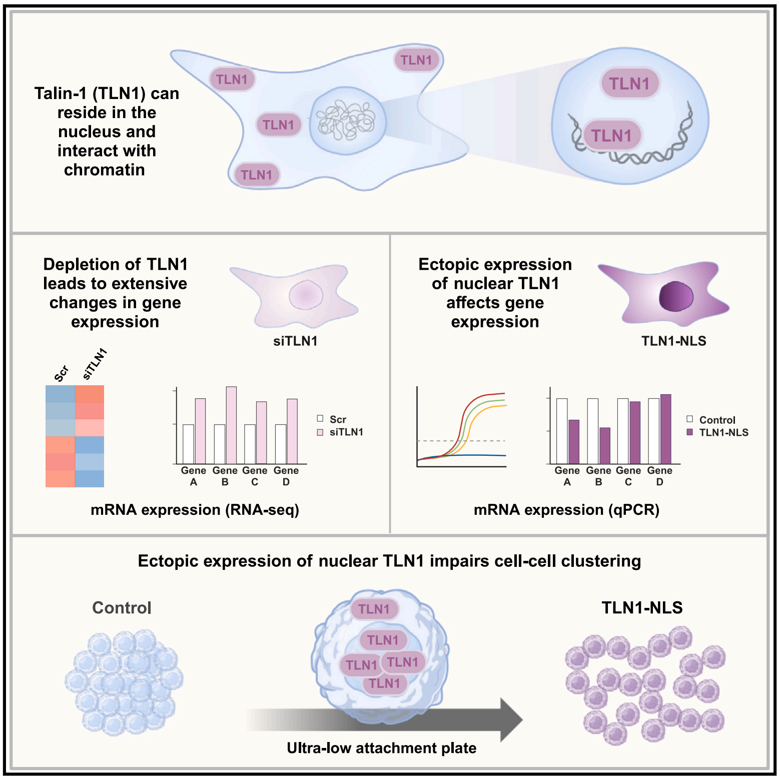

Authors

Alejandro J. Da Silva,
Hendrik S.E. Hästbacka,
Mikael C. Puustinen, ...,
Guillaume Jacquemet, Eva Henriksson,
Lea Sistonen

Correspondence

eva.henriksson@abo.fi (E.H.),
lea.sistonen@abo.fi (L.S.)

In brief

Properties of biomolecules; Cellular physiology; Molecular biology; Molecular interaction; Cell biology

Highlights

- Talin-1 (TLN1) localizes in the nucleus in several human cell lines
- TLN1 associates with the chromatin
- TLN1 depletion results in widespread alterations in gene expression
- Nuclear TLN1 affects gene expression and disrupts cell-cell clustering

Da Silva et al., 2025, iScience *28*, 111745
February 21, 2025 © 2025 The Author(s). Published by Elsevier Inc.
https://doi.org/10.1016/j.isci.2025.111745

CellPress

iScience

CellPress
OPEN ACCESS

Article

Nuclear talin-1 provides a bridge between cell adhesion and gene expression

Alejandro J. Da Silva,[1,2] Hendrik S.E. Hästbacka,[1,2] Mikael C. Puustinen,[1,2] Jenny C. Pessa,[1,2] Jens C. Luoto,[1,2] Erika Sundström,[1,2,7] Benjamin T. Goult,[3] Guillaume Jacquemet,[1,2,4,5] Eva Henriksson,[1,2,6,*] and Lea Sistonen[1,2,6,8,*]

[1]Faculty of Science and Engineering, Cell Biology, Åbo Akademi University, 20520 Turku, Finland
[2]Turku Bioscience Centre, University of Turku and Åbo Akademi University, 20520 Turku, Finland
[3]Department of Biochemistry, Cell & Systems Biology, Institute of Systems, Molecular and Integrative Biology, University of Liverpool, Crown Street, Liverpool L69 7ZB, UK
[4]InFLAMES Research Flagship Center, University of Turku and Åbo Akademi University, 20520 Turku, Finland
[5]Turku Bioimaging, University of Turku and Åbo Akademi University, 20520 Turku, Finland
[6]These authors contributed equally
[7]Deceased
[8]Lead contact
*Correspondence: eva.henriksson@abo.fi (E.H.), lea.sistonen@abo.fi (L.S.)
https://doi.org/10.1016/j.isci.2025.111745

SUMMARY

Talin-1 (TLN1) is best known to activate integrin receptors and transmit mechanical stimuli to the actin cytoskeleton at focal adhesions. However, the localization of TLN1 is not restricted to focal adhesions. By utilizing both subcellular fractionations and confocal microscopy analyses, we show that TLN1 localizes to the nucleus in several human cell lines, where it is tightly associated with the chromatin. Importantly, small interfering RNA (siRNA)-mediated depletion of endogenous TLN1 triggers extensive changes in the gene expression profile of human breast epithelial cells. To determine the functional impact of nuclear TLN1, we expressed a TLN1 fusion protein containing a nuclear localization signal. Our findings revealed that the accumulation of nuclear TLN1 alters the expression of a subset of genes and impairs the formation of cell-cell clusters. This study introduces an additional perspective on the canonical view of TLN1 subcellular localization and function.

INTRODUCTION

Accumulating evidence indicates active communication between the plasma membrane, cell cortex, and the nucleus by nuclear translocation of proteins.[1] Many of these proteins are associated with transmembrane adhesion receptors, which connect the extracellular matrix (ECM) and surface proteins of neighboring cells to the cytoskeleton.[1,2] These cell-ECM and cell-cell contacts provide cells with structural and mechanical stability, and both types of junctions act as signaling platforms that collect information from the extracellular space. Therefore, identifying proteins that mediate the communication between the cell cortex and the nucleus is pivotal to determine how cells respond to their surroundings. In a recent article, Byron and collaborators performed proteomic analyses and found that a considerable number of adhesion complex-associated proteins also reside in the nucleus.[3] However, the functions of most adhesion-associated proteins inside the nucleus remain poorly understood.

Talin-1 (TLN1) is a 270-kDa adaptor protein that is best known for its role in focal adhesion (FA) assembly.[4] FAs are structures characterized by proteins that connect actin filaments to integrin transmembrane receptors.[5] To achieve its function at the FAs, TLN1 has a particular domain structure that is composed of an N-terminal FERM (4.1 protein, ezrin, radixin, moesin) domain, known as the head domain, which is coupled to a flexible rod domain comprising 13 helical bundles.[6] The head domain interacts with the cytoplasmic tails of β-integrin subunits, whereas both the head and the rod domains bind to actin filaments and the rod domain acts as a mechanosensitive signaling hub[7] (Figure 1A, left panel). Dysregulation of TLN1 is associated with different diseases, such as cancer, cardiovascular malfunction, and hematologic disorders, which makes TLN1 a relevant protein in the context of therapeutics and diagnostics.[8–10] Interestingly, TLN1 is not confined to the FA complexes suggesting that this protein has other roles apart from the FA assembly. For example, TLN1 has been recently shown to mediate cell-cell contacts during mitosis through the activation of β1 integrin without engagement of the actin cytoskeleton.[11] TLN1 is also localized at invadopodia, which are actin-rich protrusions that mediate cancer cell invasion and metastasis, where it acts as a scaffold to recruit the sodium/hydrogen exchanger 1 protein.[12] Since TLN1 can reside in the cytoplasm where it adopts a conformation that is unable to mediate the connection between integrins and the actin cytoskeleton, it might be involved in other signaling pathways.[13,14] Consequently, characterizing the subcellular localization and function of TLN1 is fundamental for

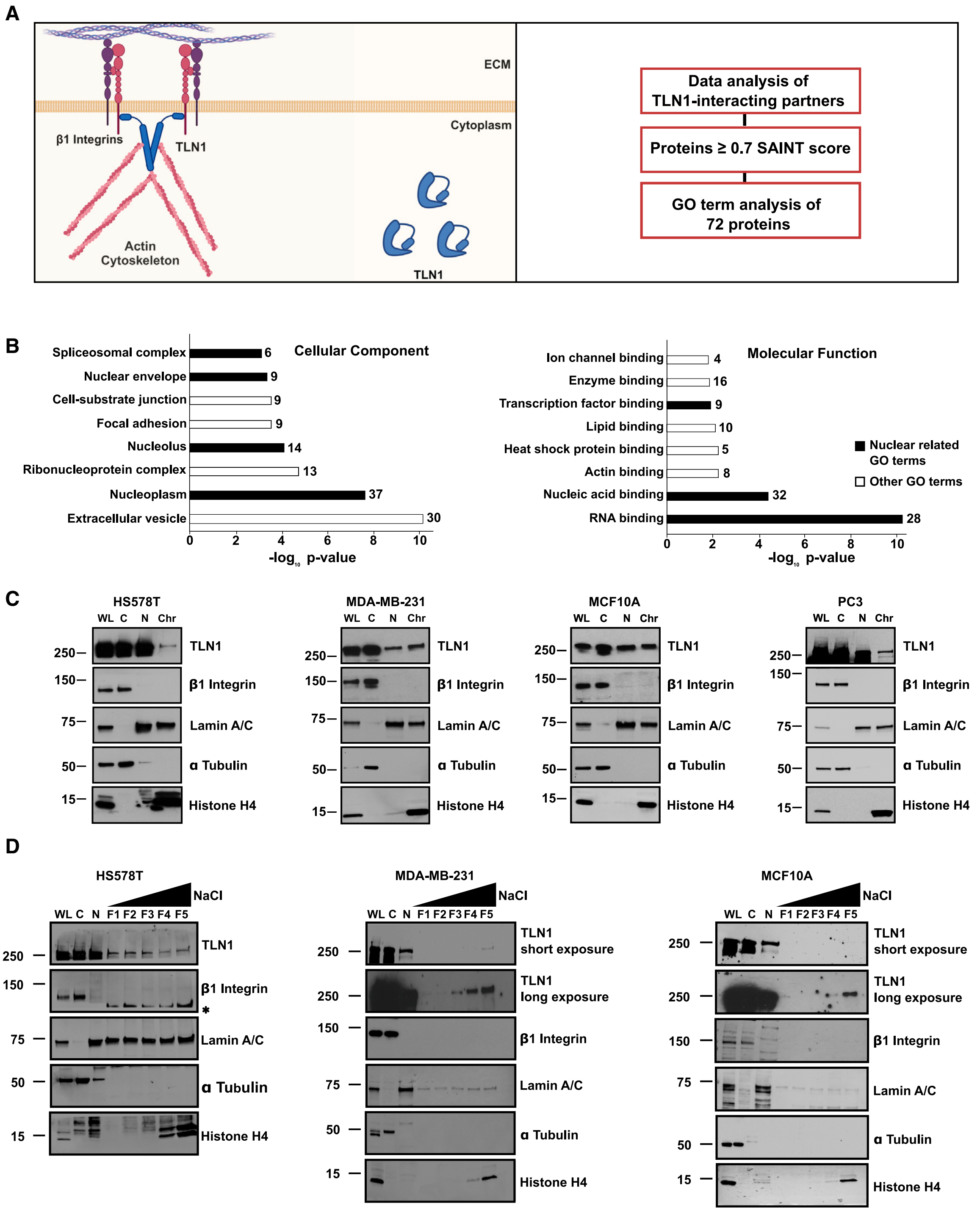

Figure 1. TLN1 is localized in the nucleus where it strongly interacts with the chromatin

(A) A schematic overview of the established subcellular localization of Talin-1 (TLN1) according to the current literature. TLN1 is localized in the focal adhesions and the cytoplasm (left). Analysis of TLN1-interacting partners previously identified by Gough and collaborators (right).[15] Made in BioRender.com.

(B) Gene ontology (GO) terms associated with TLN1-interacting partners were analyzed with the online application ShinyGO. The GO terms within the "cellular component" and "molecular function" ontologies were ranked according to their *p* values and the redundant terms were withdrawn. The number of proteins associated with each term is indicated, and terms composed of less than four proteins are not shown. GO terms related to the nucleus are highlighted in black.

(legend continued on next page)

understanding its impact in physiological processes and pathological states.

In this study, we investigated the subcellular localization of TLN1. Biochemical analyses showed, to our surprise, that TLN1 can also localize to the nuclei of human epithelial cells, where it is tightly associated with the chromatin. The nuclear localization of TLN1 was corroborated by confocal microscopy analyses. Moreover, small interfering RNA (siRNA)-mediated TLN1 depletion resulted in extensive changes in the gene expression profile of breast epithelial cells, causing upregulation and downregulation of approximately 300 and 400 genes, respectively. To investigate the role of nuclear TLN1 in gene expression, we generated a fusion protein composed of the full-length human TLN1 coupled to GFP and a nuclear localization signal (NLS). By ectopically expressing the TLN1-NLS fusion protein, we demonstrate that enriching TLN1 in the nucleus modifies the expression of a subset of genes and impairs the capability of cells to form clusters with each other. Taken together, this study identifies TLN1 as a nuclear protein that impacts gene expression and disrupts cell-cell associations upon accumulation in the nucleus.

RESULTS

TLN1 is localized in the nucleus where it is tightly associated with the chromatin

To initiate the study on the subcellular localization of TLN1, we examined the Gene Ontology (GO) terms associated with TLN1-interacting proteins, which were identified in a recently published mass spectrometry screen[15] (Figure 1A, right panel). Gough and collaborators determined the probability of *bona fide* protein-protein interactions by calculating the Significance Analysis of INTeractome (SAINT) score, and a total of 72 TLN1-interacting partners, which had a SAINT score ≥ 0.7, were chosen for our GO term analysis. Interestingly, the analysis revealed that a majority, i.e., 37, of these 72 proteins are associated with the nucleus (Figure 1B) (Table S1). These results are in agreement with the subcellular proteomics study of Byron and collaborators, who found TLN1 to reside in the nucleus together with other adhesion-related proteins, which they collectively defined as the nucleo-adhesome.[3] In addition, we used the BioGRID database to search for other interactome studies in which TLN1 could be identified as a putative interacting partner of nuclear proteins.[16] Remarkably, we found several studies performed with nuclear extracts where TLN1 was identified as a partner of cell division cycle 5-like protein/SNW domain-containing 1, minichromosome maintenance complex component 2 (MCM2), and peroxisome proliferator-activated receptor gamma[17–19] (Table S2). Of these proteins, we validated MCM2 as a TLN1-interacting partner using proximity ligation assay, which allows the visualization of protein complexes in different subcellular compartments (Figure S1A). Our results revealed that TLN1 and MCM2 interact in the cytoplasm and nucleus of human osteosarcoma U2OS cells (Figure S1A).

These findings prompted us to investigate whether TLN1 is localized in the nucleus of transformed (HS578T and MDA-MB-231) and non-transformed (MCF10A) human breast epithelial cells, as well as transformed human prostate epithelial cells (PC3) (Figure 1C). To achieve fractions of high purity, we utilized a protocol based on stepwise cell lysis where the cytoplasm is separated from the intact nucleus, which in turn is lysed separately to extract proteins located either in the nucleoplasm or in the chromatin. To assess the purity of the subcellular fractions, we monitored the localization of proteins that are known to reside in the plasma membrane (β1 integrin), cytoplasm (α-tubulin), nucleus (lamin A/C), and chromatin (histone H4).[20–22] The results showed that the control proteins were clearly enriched in their corresponding fractions, demonstrating the efficacy of the subcellular fractionation protocol (Figure 1C). In accordance with the aforementioned mass spectrometry data analyses, we found that TLN1 co-purifies with the nuclear and chromatin-associated fractions of all the cell lines tested. Next, we addressed whether trypsin detachment of cells prior to subcellular fractionation had an effect on the nuclear localization of TLN1. By comparing the subcellular fractions of MDA-MB-231 cells with and without trypsin treatment (Figure S1B), we observed the nuclear localization of TLN1 regardless of the treatment.

To evaluate the strength of TLN1's association with the chromatin, we conducted differential salt fractionations. The pellet, which remained after collecting the nuclear fraction, was incubated with increasing concentrations of NaCl (0.3, 0.45, 0.6, 0.8, and 1.2 M) to release chromatin-bound proteins. Proteins weakly associated with chromatin (e.g., transcription factors) are soluble in low concentrations of NaCl, while proteins tightly associated with chromatin (e.g., histones) are only displaced at high concentrations of NaCl.[20] In MCF10A and MDA-MB-231 cells, TLN1 co-eluted with histone H4 at the highest concentrations of the NaCl, whereas in HS578T cells, TLN1 co-eluted with lamin A/C throughout the NaCl gradient (Figure 1D), indicating a weaker affinity for the chromatin. These data suggest that the strength of the TLN1-chromatin association varies among cell lines, potentially due to differences in the identity of TLN1-interacting partners in these cells.

To corroborate our results with an approach that involves the minimal disruption of cell integrity, we performed indirect immunofluorescence staining of TLN1 in HS578T and MDA-MB-231 cells. For this, we used a TLN1-specific antibody (TA205), which recognizes the head domain of TLN1.[23,24] The expected localization of TLN1 in the FAs was observed at the bottom plane of the cells, while visualizing a single focal plane in the middle of the z stack displayed nuclear TLN1 signal in both cell lines

(C) Immunoblot analysis of TLN1 in subcellular fractionations of HS578T, MDA-MB-231, MCF10A, and PC3 cells. WL, whole-cell lysate; C, cytoplasmic fraction; N, nuclear fraction; Chr, chromatin fraction. To monitor the purity of the fractionation protocol, the following controls were used: β1 integrin (plasma membrane), lamin A/C (nucleus), α-tubulin (cytoplasm), histone H4 (chromatin).

(D) Immunoblot analysis of TLN1 in differential salt fractionation of HS578T, MDA-MB-231, and MCF10A cells. F1: 0.3, F2: 0.45, F3: 0.6, F4: 0.8, and F5: 1.2 M of NaCl. The fractionation controls were the same as in (C), and remnant signal from a previous lamin A/C immunoblot is indicated with an asterisk (*). See also Tables S1 and S2.

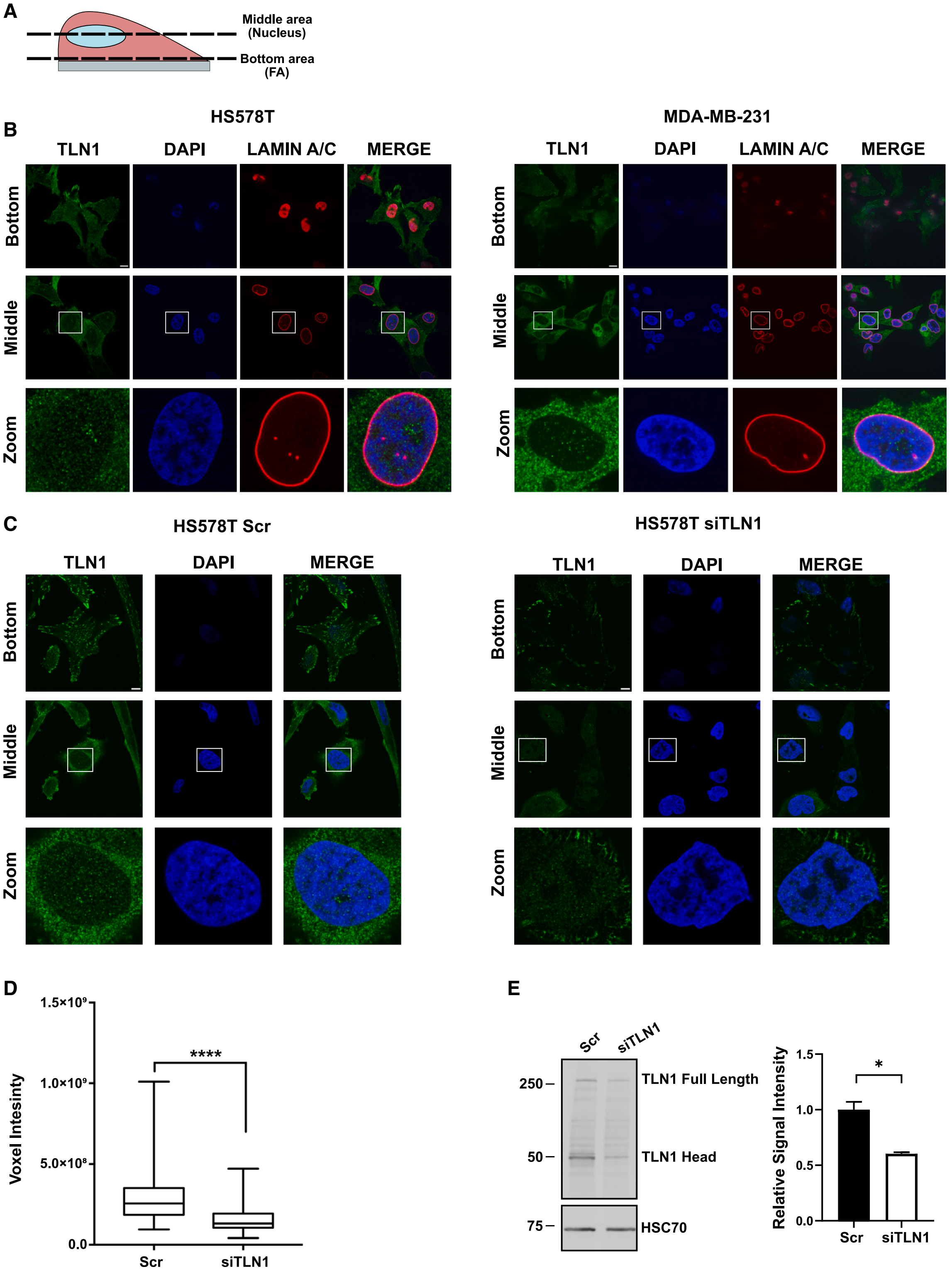

Figure 2. Nuclear TLN1 immunofluorescence signal is reduced upon TLN1 depletion

(A) A schematic overview of single focal planes shown in (B) and (C).

(B) Confocal microscopy images of TLN1 immunofluorescence staining in HS578T and MDA-MB-231 cells. Scale bar 10 μm.

(C) Confocal microscopy images of TLN1 immunofluorescence staining in HS578T transfected with either Scr or siTLN1 RNA. Lamin A/C and DAPI were used as nuclear markers. Scale bar 10 μm. All images are representative of three biological replicates.

(legend continued on next page)

(Figures 2A and 2B). Furthermore, we verified the specificity of the immunofluorescence staining by silencing TLN1 in HS578T cells with a combination of two siRNAs specific for TLN1 (siTLN1) (Figure 2C). Cells transfected with the siTLN1 showed a clear reduction of the total immunofluorescence signal compared to the Scr control. Importantly, the TLN1-depleted cells were still able to maintain cell adhesion in culture, consistent with the findings of Wang and collaborators, who showed that even low levels of residual TLN1 are sufficient to prevent cellular detachment.[25] Three-dimensional quantification of the immunofluorescence signal inside the nucleus of TLN1-depleted cells confirmed the loss of TLN1 nuclear signal (Figure 2D). Immunoblotting analyses of the same samples used for immunofluorescence showed reduced levels of TLN1 upon siTLN1 treatment, further corroborating the specificity of the TLN1 antibody used (Figures 2E and S1C). Taken together, our results demonstrate that TLN1 is localized in the nucleus, where it is tightly associated with the chromatin.

Interestingly, vertebrates have two talin isoforms, TLN1 and TLN2, of which TLN1 exhibits a ubiquitous expression pattern while TLN2 is expressed only in certain cell types.[4] Therefore, we analyzed the protein levels of both talin isoforms in HS578T, MDA-MB-231, MCF10A, and PC3 cells by performing a mass spectrometry analysis (Figure S1D; Table S3). The analysis showed that in all cell lines, the levels of TLN1 were drastically higher than TLN2, and we decided to focus on TLN1 in this study. However, we do not rule out the possibility that TLN2 could also be present in the nucleus.

Nuclear TLN1 affects gene expression

The nuclear localization of TLN1 prompted us to investigate whether downregulation of the total TLN1 levels modifies the gene expression profile of HS578T cells. To this end, we downregulated TLN1 with siRNA and analyzed the global gene expression profile with RNA sequencing (RNA-seq) (Figures 3A and 3B). Differentially expressed (DE) genes between the Scr and siTLN1-transfected cells were determined with the Bioconductor R package edgeR,[26] using a $\log_2$ fold change of at least ±0.5 and a false discovery rate (FDR) < 0.05 from two biological replicates. Depletion of TLN1 caused extensive changes in the gene expression profile of HS578T cells, resulting in the upregulation of 318 genes and the downregulation of 419 genes (Figure 3C) (Table S4). Notably, TLN1 was the most significantly downregulated gene in our RNA-seq screen, thereby confirming the efficacy of the silencing method (Figure 3C, right panel). Normalized gene expression data were used to generate heatmaps from the top 25 upregulated and 25 downregulated DE genes (Figure 3D). In line with the well-known functions of TLN1 as a mechanosensitive adaptor protein in FAs, we found several TLN1-dependent genes that are involved in cell adhesion (Figure 3E). Among the DE genes, we also identified genes related to nuclear functions, such as those encoding nuclear structural proteins (NEMP1 and H2BC4), chromatin remodelers (BCL7B and MORF4L1), and transcription factors (NFATC2) (Figure 3F).

Due to the key role of TLN1 in the FA complexes, it is possible that some of the changes in gene expression upon TLN1 depletion are caused by the disruption of FA-dependent signaling pathways. For instance, it has been shown that phosphorylated focal adhesion kinase (FAK), a well-established marker of integrin activation, regulates gene expression.[27] However, no clear change in the levels of either phosphorylated or total FAK protein was observed upon TLN1 silencing (Figure 3B). To determine whether nuclear TLN1 affects gene expression, we enriched the amount of nuclear TLN1 and determined the mRNA levels of five TLN1-dependent genes: SEMA7A, NFATC2, ACTG1, BCL7B, and SEC23A (Figures 3D and 4B). For this purpose, we constructed a fusion protein consisting of the full-length human TLN1 coupled with GFP and an NLS (TLN1-NLS). HS578T cells were transfected with the TLN1-NLS construct, and GFP-NLS was used as the corresponding control. Analysis with confocal microscopy confirmed that both the TLN1-NLS and GFP-NLS fusion proteins were localized inside the nucleus (Figure 4A). Next, the mRNA levels of the five TLN1-dependent genes were examined in the GFP-NLS and TLN1-NLS-transfected cells with quantitative reverse-transcription PCR (qRT-PCR) (Figure 4B). In line with our RNA-seq data, enriching TLN1 in the nucleus shifted the expression of SEMA7A and NFATC2 in an opposite pattern to that observed upon TLN1 depletion (Figures 3D and 4B). In contrast, the expression of ACTG1, BCL7B, and SEC23A remained unchanged irrespective of the amount of nuclear TLN1, showing that not all TLN1-dependent genes are responsive to fluctuations in nuclear TLN1 levels (Figure 4B). Therefore, our results provide a proof of concept that nuclear TLN1 affects gene expression, and future studies are required to comprehensively identify the gene expression profile that is dependent on nuclear TLN1.

To explore the functional impact of nuclear TLN1, in addition to its role in gene expression, we performed a GO term analysis of the 737 TLN1-dependent genes (Table S5). Congruent with the role of TLN1 in the formation of FAs, we observed that cell adhesion was among the enriched ontologies. Of note, a considerable number of the cell adhesion genes were associated with cell-cell adhesion and the cytoskeleton (Figure 4C). Prompted by this finding, we tested the capability of GFP and TLN1-NLS-transfected HS578T cells to form cell clusters using ultra-low attachment round-bottom plates. Remarkably, cells transfected with the TLN1-NLS construct failed to form compact spheroid-like structures when compared to the GFP-transfected counterparts, as evidenced by the difference in areas of cell conglomerates analyzed under both conditions (Figure 4D). Taken together, our results demonstrate that nuclear TLN1 has a functional impact on gene expression and that the enrichment of nuclear

---

(D) Quantification of voxel intensity values within the nucleus. The data whiskers represent minimum and maximum values. The statistical significance was analyzed with a Mann-Whitney test; **** p value <0.0001. The data represent three biological replicas, 98–132 nuclei in total.

(E) Immunoblot analysis of TLN1 expression in HS578T cells transfected with either Scr or siTLN1. HSC70 was used as a loading control (left). The whole lane intensity in the TLN1 blot was normalized to the respective HSC70 level. The data are presented as mean values + SD of three biological replicas. The statistical significance was analyzed with two-tailed Student's t test; *p value < 0.05. See also Figure S1C.

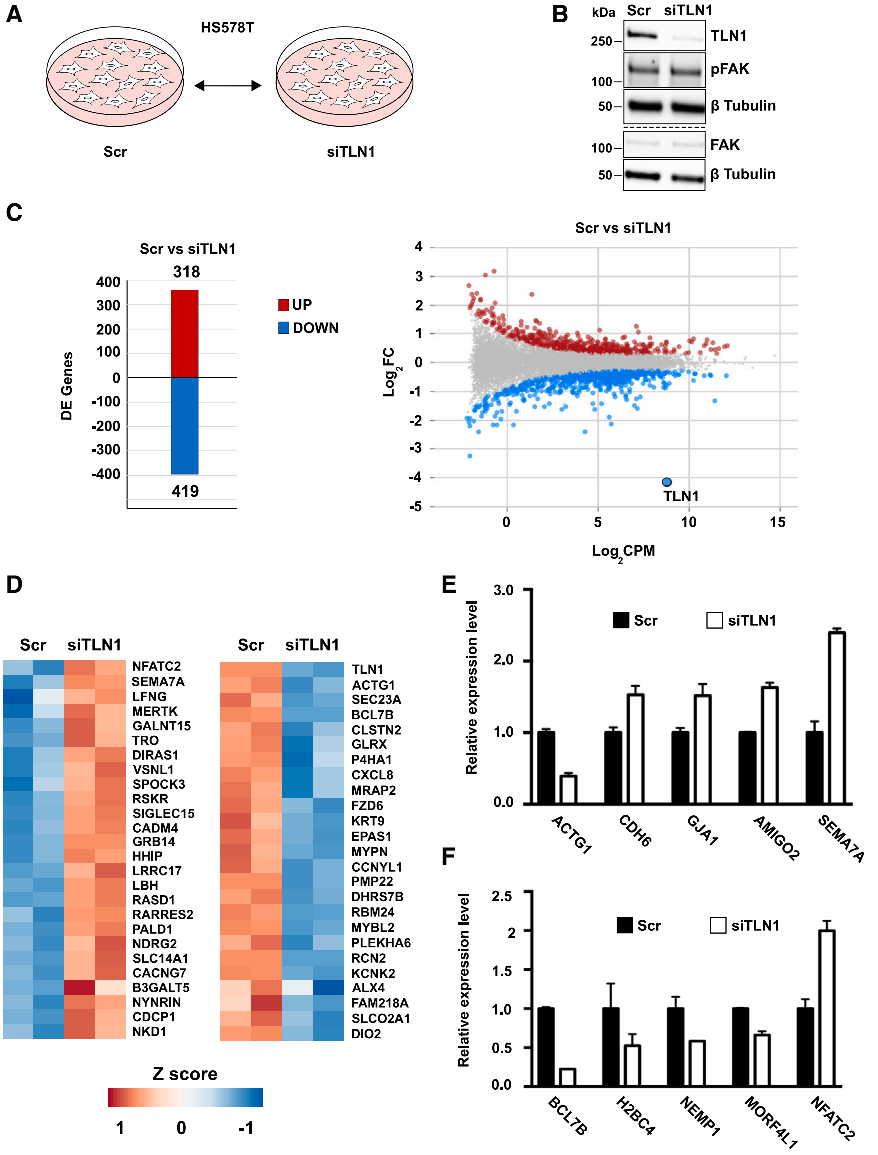

Figure 3. Depletion of TLN1 triggers extensive changes in gene expression

(A) A schematic overview of the experimental setup for RNA-seq. HS578T cells were transfected with either Scr or siTLN1, and the total RNA from each cell population was extracted and analyzed by RNA-seq. The arrows depict the comparison made for the RNA-seq analysis.

(B) Immunoblot analysis of TLN1, FAK, and phosphorylated FAK (pFAK) levels in HS578T cells transfected with either Scr or siTLN1. β-tubulin was used as a loading control. The dotted line denotes blots from two distinct membranes with the same samples. Two biological replicas were used for this experiment.

(C) Differentially expressed (DE) genes in the Scr vs. siTLN1 comparison were determined by Bioconductor R package edgeR[26] (log_2 FC at least ±0.5; FDR < 0.05). The number of upregulated and downregulated genes are indicated with red and blue bars, respectively (left). Individual DE genes between the Scr and siTLN1 samples were visualized in an MA plot. TLN1 is highlighted (right).

(D) The top 50 DE genes were used to generate heatmaps with the CRAN R package pheatmap. The top 25 upregulated and downregulated genes are shown in the left and right, respectively.

(E and F) Relative expression levels of five DE genes related to cell adhesion (E) and nuclear functions (F). Error bars +SD. Note that these genes were chosen from the list of total DE genes, see also Table S4.

TLN1 impairs the capability of cells to form proper cell-cell associations.

DISCUSSION

The function of TLN1 as a mechanosensitive adaptor protein in integrin adhesion complexes is extensively characterized and continues to be the major focus in the field of TLN1 research. Nevertheless, roles of TLN1 in other cellular compartments have remained enigmatic, which prompted us to investigate the subcellular localization of TLN1. To our surprise, both biochemical and confocal microscopy analyses showed that TLN1 also resides in the nucleus where it is tightly associated with chromatin. RNA-seq analysis revealed that the depletion of TLN1 results in extensive changes in the gene expression profile of human breast epithelial cells. Finally, by enriching TLN1 in the nucleus, we demonstrate that increased levels of nuclear TLN1 impact the expression of a specific subset of the TLN1-dependent genes and impair the proper formation of cell-cell associations as illustrated in our model (Figure 5).

Active communication between the cell cortex and the nucleus is essential to ensure a coordinated transcriptional response upon extracellular stimuli.[1] Among the proteins that participate in the FAs, zyxin, paxillin, and FAK have been shown to translocate to the nucleus and regulate gene expression.[28,29] Intriguingly, studies centered on FAK have led to the hypothesis that FERM domain-containing proteins act as information mediators between the plasma membrane and the nucleus.[30] Similarly, TLN1 could translocate from the cell cortex to the nucleus to regulate gene expression in response to extracellular stimuli. However, further studies are required to determine the specific mechanisms that mediate the nuclear translocation of TLN1.

In the light of our results, it is interesting to consider how nuclear TLN1 is capable of regulating gene expression. Previously, it has been shown that nuclear FAK controls chromatin accessibility to allow the binding of transcription factors to specific genomic loci.[31] In addition, nuclear localization of both actin and myosin-1C, which were initially thought to be strictly

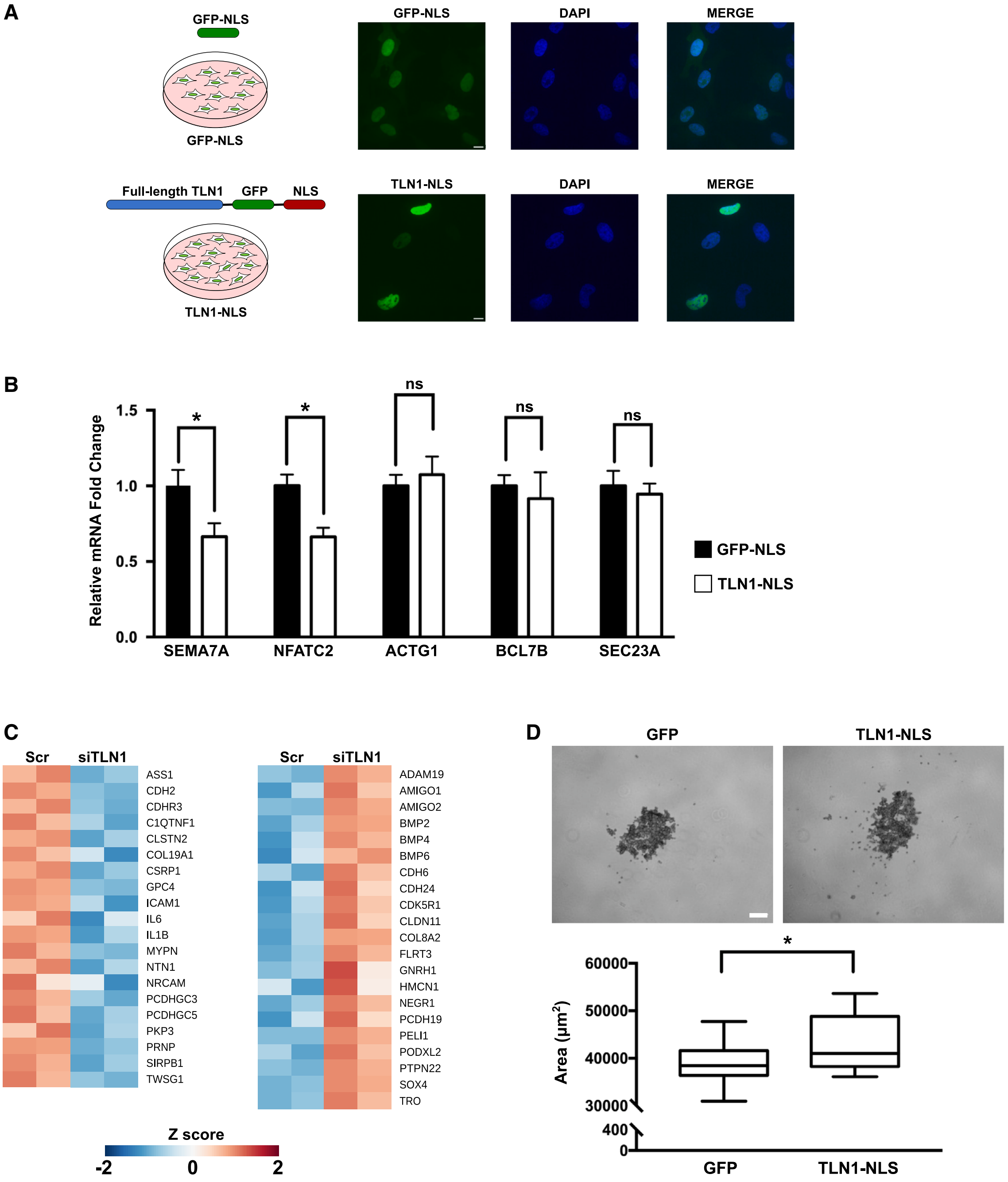

Figure 4. Nuclear TLN1 affects gene expression

(A) A schematic overview of the experimental setup to test the role of nuclear TLN1 for gene expression in HS578T cells (left). Confocal microscopy images corresponding to maximum intensity projections of the fluorescent signal emitted by GFP-NLS or the TLN1-NLS construct (right). Scale bar 10 μm.

(B) mRNA expression of semaphorin 7A (SEMA7A), nuclear factor of activated T cell 2 (NFATC2), actin gamma 1 (ACTG1), BAF chromatin remodeling complex subunit BCL7B (BCL7B), and SEC23 homolog A (SEC23A) in HS578T cells. The mRNA levels were quantified with qRT-PCR, and GAPDH was used as a housekeeping gene. The data are presented as mean values + SEM of three biological replicates. The statistical significance was analyzed with paired two-tailed Student's t test; ns: not significant, *p value < 0.05.

(C) Differentially expressed (DE) genes between the Scr and siTLN1 comparison pair within the GO term cell-cell adhesion. Upregulated and downregulated genes are shown in the left and right, respectively.

(D) Representative images of spheroid-like structures in ultra-low attachment plates, scale bar 100 μm (upper). Quantitative analysis of spheroid area (lower). The relative area was quantified in Fiji (ImageJ, version: 1.53t), using the BioVoxxel Toolbox plugin. Results were plotted with mean ± SEM from three biological replicates, 20–23 spheroid images in total. The statistical significance was analyzed with two-tailed Student's t test; *p value < 0.05. See also Table S5.

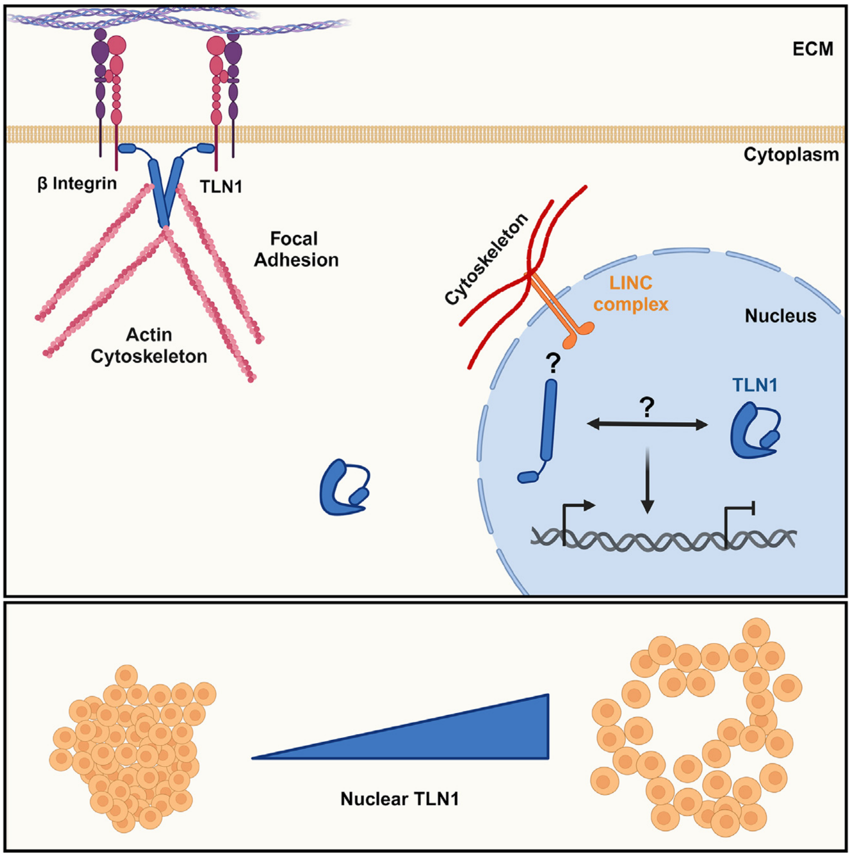

Figure 5. Model of the subcellular localization of TLN1 and its impact on cell-cell adhesion

Aside from the focal adhesions and cytoplasm, TLN1 is present in the nucleus, where it associates with the chromatin, causing changes in gene expression programs. TLN1 is represented in open and closed conformations in different subnuclear locations, but the precise conformation of nuclear TLN1 remains to be determined. It is plausible that nuclear TLN1 interacts with the LINC complex and that it responds to mechanical stimuli in the nucleus through interacting with proteins of this complex (upper). Finally, cells with enriched levels of nuclear TLN1 exhibit a lower capability to form cell-cell contacts when compared to cells where nuclear TLN1 is not enriched (lower). Made with BioRender.com.

cytoplasmic proteins, alter chromatin landscape, and they also cooperate to maintain active RNA polymerase II at gene promoters.[32,33] Our results demonstrate that TLN1 is tightly associated with the chromatin of human epithelial cells, suggesting that it could function in a similar manner as nuclear actin, nuclear myosin-1C, and/or nuclear FAK. Here, we also validated the nuclear interaction between TLN1 and the MCM2, a protein that has been shown to bind histones and impact transcription during differentiation of mouse embryonic stem cells.[34] Furthermore, we recently reported that TLN1 interacts with heat shock factor 2, a transcription factor that plays an important role in cell-cell adhesion.[35,36] Therefore, it is tempting to speculate that nuclear TLN1 is part of protein networks to regulate gene expression and/or chromatin architecture. This is also supported by the finding of 32 DNA-binding proteins as high-confidence (SAINT score ≥ 0.7) putative interacting partners in the mass spectrometry screen of Gough and collaborators (Figure 1B). Interestingly, the same screen also identified 14 nucleolar proteins. Given that our immunofluorescence staining for TLN1 showed signal accumulation in the dark areas of the DAPI staining in some cells, it is plausible that a portion of the nuclear TLN1 pool is also localized within the nucleolus.

Enriching the levels of nuclear TLN1 impaired the capacity of cells to form clusters with each other. This phenomenon suggests that TLN1 is involved in the intricate crosstalk between cell-substrate and cell-cell adhesions, which is pivotal in normal physiological states and various disease conditions. For instance, during the process of epithelial-to-mesenchymal transition, which takes place during wound healing and cancer metastasis, cells increase their motility by enhancing their cell-matrix adhesions and by destabilizing their cell-cell junctions.[37] Strikingly, overexpression of TLN1 increases cell-matrix adhesion, cell motility, and the invasion capacity of different types of cancer cells.[10] Therefore, forthcoming studies are warranted to investigate whether the enrichment of nuclear TLN1 facilitates the escape of cancer cells from the primary tumor by impairing cell-cell connections.

Due to the mechanosensitive role of TLN1 in FA complexes, it is important to consider whether nuclear TLN1 might also respond to mechanical stimuli. In the past few years, extensive research has explored how the nucleus reacts to mechanical forces from the extracellular space as well as the intracellular cytoskeleton.[38] Among the best characterized mechanisms of nuclear mechanosensitivity is the protein machinery known as the linker of nucleoskeleton and cytoskeleton (LINC) complex.[39] The LINC complex connects the nuclear envelope with the contractile cytoskeleton, and this physical connection mediates the transmission of force to proteins in the inner periphery of the nuclear envelope including nuclear lamins.[40,41] Curiously, the rod domain of TLN1 is composed of 13 α-helical bundles that function as mechanosensitive switches, which change their conformation to expose binding sites for different interacting partners.[7] Thus, one can hypothesize that TLN1 acts as a nuclear mechanosensitive signaling hub connecting the LINC complex to the chromatin, thereby regulating gene expression (Figure 5). In support of this view, our analysis of the existing mass spectrometry data[15] revealed that TLN1 putatively interacts with nine proteins associated with the nuclear envelope, including emerin, which mediates changes in nuclear stiffness upon stimulation of the LINC complex.[38]

In summary, we substantiate that TLN1 also resides in the nucleus, and we report unexpected properties of TLN1 by showing that it can be associated with the chromatin and that nuclear TLN1 affects gene expression. Our study extends the canonical view of TLN1 subcellular localization and function.

Limitations of the study

This study challenges the conventional understanding of TLN1 subcellular localization and function. Our research revealed the localization of TLN1 in the nucleus, where it is associated with the chromatin. However, due to the qualitative nature of the fractionation protocol used in this study, our approach does not measure the proportion of TLN1 that is present in the nucleoplasm or associated with the chromatin in comparison to the cytoplasmic TLN1 pool. Furthermore, we demonstrated that TLN1 affects gene expression and the enrichment of TLN1 in the nucleus impairs cell-cell association. Although our results showed the presence of TLN1 in the nucleoplasm and chromatin, the precise regulatory mechanisms governing TLN1 translocation to the nucleus, its role in gene expression, and cell-cell association remain to be uncovered. Specifically, determining the conformation of TLN1 in the nucleus and whether nuclear TLN1 responds to mechanical stimuli are important future research topics as raised by our discoveries. Moreover, as we also identified a set of genes that exhibit differential expression patterns upon the overall TLN1 silencing, it will be crucial to discern the distinct effects of the nuclear vs. cytoplasmic TLN1 on global gene expression programs. Importantly, we cannot rule out that increasing the levels of nuclear-TLN1 could affect gene expression by altering the mechanosensing dynamics of the nucleus or the structure of focal adhesions and ECM deposition. Future studies are called for to reveal the underlying mechanisms.

RESOURCE AVAILABILITY

Lead contact

Further information and requests for resources and reagents should be directed to and will be fulfilled by the lead contact, Lea Sistonen (lea.sistonen@abo.fi). The resources are shared for research and educational purposes without restriction.

Materials availability

All plasmids and cell lines generated in this study are available from the authors upon request.

Data and code availability

- The RNA-seq dataset is available at the Gene Expression Omnibus (GEO) under the accession number GSE198191. The mass spectrometry proteomics data have been deposited to the ProteomeXchange Consortium via the PRIDE partner repository[42] under the accession number PXD058465.
- This paper does not report original code.
- Any additional information required to reanalyze the data reported in this paper is available from the lead contact upon request.

ACKNOWLEDGMENTS

We thank all the members of Sistonen laboratory for expert support during the preparation of the manuscript. The Cell Imaging and Cytometry Core facility (Turku Bioscience, University of Turku, Åbo Akademi University, and Biocenter Finland) and Turku Bioimaging are acknowledged for services, instrumentation, and expertise. We thank Markku Saari, Jouko Sandholm, and Christoffer Lagerholm from the Cell Imaging Core of Turku Bioscience Center for technical assistance and advice. We thank Joanna Pylvänäinen for her assistance with image analysis. Mass spectrometry analyses were performed at the Turku Proteomics Facility supported by Biocenter Finland. The Finnish Functional Genomics Center (Turku Bioscience, University of Turku, Åbo Akademi University and Biocenter Finland) is acknowledged for services, instrumentation, and expertise.

This work has been funded by the Research Council of Finland (338537 to G.J. and 355596 to L.S.), Sigrid Jusélius Foundation (G.J. and L.S.), Cancer Foundation Finland (G.J. and L.S.), Centre for International Mobility (A.J.D.S. and E.H.), Ella and Georg Ehrnrooth Foundation (A.J.D.S. and H.S.E.H.), Finnish Cultural Foundation (A.J.D.S.), K. Albin Johansson Foundation (A.J.D.S. and E.H.), InFLAMES Flagship Programme of the Research Council of Finland (decision numbers: 337530, 337531, 357910, and 357911 to G.J.), Magnus Ehrnrooth Foundation (A.J.D.S., J.C.L., and E.H.), Medicinska Understödsföreningen Liv och Hälsa r.f. (A.J.D.S., E.H., and L.S.), Otto A. Malm Foundation (A.J.D.S.), The Maud Kuistila Memorial Foundation (H.S.E.H.), Solutions for Health strategic funding to Åbo Akademi University (G.J.), and Åbo Akademi University (A.J.D.S., J.C.P., and L.S.).

AUTHOR CONTRIBUTIONS

A.J.D.S., E.H., and L.S. designed the research. A.J.D.S., H.S.E.H., M.C.P., J.C.P., J.C.L., E.S., and E.H. performed experiments. H.S.E.H. analyzed the RNA-seq data. A.J.D.S., H.S.E.H., M.C.P., J.C.P., B.T.G., G.J., E.H., and L.S. interpreted the data. A.J.D.S., H.S.E.H., E.H., and L.S. wrote the manuscript with the contribution of all the authors.

DECLARATION OF INTERESTS

The authors declare no competing interests.

STAR★METHODS

Detailed methods are provided in the online version of this paper and include the following:

- KEY RESOURCES TABLE
- EXPERIMENTAL MODEL AND STUDY PARTICIPANT DETAILS
  - Cell lines
- METHOD DETAILS
  - Transfections and gene silencing
  - Plasmid construction
  - Gene ontology (GO) term analysis
  - Subcellular fractionations
  - Differential salt fractionation
  - Immunoblotting
  - Immunofluorescence and confocal microscopy
  - Proximity ligation assay (PLA)
  - Mass spectrometry
  - RNA-sequencing
  - Quantitative RT-PCR (qRT-PCR)
  - Ultra-low attachment assay
- QUANTIFICATION AND STATISTICAL ANALYSIS

SUPPLEMENTAL INFORMATION

Supplemental information can be found online at https://doi.org/10.1016/j.isci.2025.111745.

Received: August 9, 2023
Revised: February 22, 2024
Accepted: January 2, 2025
Published: January 4, 2025

REFERENCES

1. Zheng, H.C., and Jiang, H.M. (2022). Shuttling of cellular proteins between the plasma membrane and nucleus (Review). Mol. Med. Rep. *25*, 14. https://doi.org/10.3892/mmr.2021.12530.
2. Hintermann, E., and Christen, U. (2019). The many roles of cell adhesion molecules in hepatic fibrosis. Cells *8*, 1503. https://doi.org/10.3390/cells8121503.
3. Byron, A., Griffith, B.G.C., Herrero, A., Loftus, A.E.P., Koeleman, E.S., Kogerman, L., Dawson, J.C., McGivern, N., Culley, J., Grimes, G.R., et al. (2022). Characterisation of a nucleo-adhesome. Nat. Commun. *13*, 3053. https://doi.org/10.1038/s41467-022-30556-5.
4. Gough, R.E., and Goult, B.T. (2018). The tale of two talins – two isoforms to fine-tune integrin signalling. FEBS Lett. *592*, 2108–2125. https://doi.org/10.1002/1873-3468.13081.
5. Case, L.B., and Waterman, C.M. (2015). Integration of actin dynamics and cell adhesion by a three-dimensional, mechanosensitive molecular clutch. Nat. Cell Biol. *17*, 955–963. https://doi.org/10.1038/ncb3191.
6. Goult, B.T., Zacharchenko, T., Bate, N., Tsang, R., Hey, F., Gingras, A.R., Elliott, P.R., Roberts, G.C.K., Ballestrem, C., Critchley, D.R., and Barsukov, I.L. (2013). RIAM and vinculin binding to talin are mutually exclusive and regulate adhesion assembly and turnover. J. Biol. Chem. *288*, 8238–8249. https://doi.org/10.1074/jbc.M112.438119.
7. Goult, B.T., Brown, N.H., and Schwartz, M.A. (2021). Talin in mechanotransduction and mechanomemory at a glance. J. Cell Sci. *134*, jcs258749-7. https://doi.org/10.1242/jcs.258749.
8. Azizi, L., Cowell, A.R., Mykuliak, V.V., Goult, B.T., Turkki, P., and Hytönen, V.P. (2021). Cancer associated talin point mutations disorganise cell adhesion and migration. Sci. Rep. *11*, 347. https://doi.org/10.1038/s41598-020-77911-4.
9. Li, Y., Gao, S., Han, Y., Song, L., Kong, Y., Jiao, Y., Huang, S., Du, J., and Li, Y. (2021). Variants of focal adhesion scaffold genes cause thoracic aortic aneurysm. Circ. Res. *128*, 8–23. https://doi.org/10.1161/CIRCRESAHA.120.317361.
10. Haining, A.W.M., Lieberthal, T.J., and Del Río Hernández, A. (2016). Talin: a mechanosensitive molecule in health and disease. FASEB J. *30*, 2073–2085. https://doi.org/10.1096/fj.201500080R.
11. Huber, M., Casares-Arias, J., Fässler, R., Müller, D.J., and Strohmeyer, N. (2023). In mitosis integrins reduce adhesion to extracellular matrix and strengthen adhesion to adjacent cells. Nat. Commun. *14*, 1–17. https://doi.org/10.1038/s41467-023-37760-x.
12. Beaty, B.T., Wang, Y., Bravo-Cordero, J.J., Sharma, V.P., Miskolci, V., Hodgson, L., and Condeelis, J. (2014). Talin regulates moesin-NHE-1 recruitment to invadopodia and promotes mammary tumor metastasis. J. Cell Biol. *205*, 737–751. https://doi.org/10.1083/jcb.201312046.
13. Haage, A., Goodwin, K., Whitewood, A., Camp, D., Bogutz, A., Turner, C.T., Granville, D.J., Lefebvre, L., Plotnikov, S., Goult, B.T., and Tanentzapf, G. (2018). Talin autoinhibition regulates cell-ECM adhesion dynamics and wound healing in vivo. Cell Rep. *25*, 2401–2416.e5. https://doi.org/10.1016/j.celrep.2018.10.098.
14. Goult, B.T., Xu, X.P., Gingras, A.R., Swift, M., Patel, B., Bate, N., Kopp, P.M., Barsukov, I.L., Critchley, D.R., Volkmann, N., and Hanein, D. (2013). Structural studies on full-length talin1 reveal a compact auto-inhibited dimer: Implications for talin activation. J. Struct. Biol. *184*, 21–32. https://doi.org/10.1016/j.jsb.2013.05.014.
15. Gough, R.E., Jones, M.C., Zacharchenko, T., Le, S., Yu, M., Jacquemet, G., Muench, S.P., Yan, J., Humphries, J.D., Jørgensen, C., et al. (2021). Talin mechanosensitivity is modulated by a direct interaction with cyclin-dependent kinase-1. J. Biol. Chem. *297*, 100837. https://doi.org/10.1016/j.jbc.2021.100837.
16. Stark, C., Breitkreutz, B.J., Reguly, T., Boucher, L., Breitkreutz, A., and Tyers, M. (2006). BioGRID: a general repository for interaction datasets. Nucleic Acids Res. *34*, D535–D539. https://doi.org/10.1093/nar/gkj109.
17. Llères, D., Denegri, M., Biggiogera, M., Ajuh, P., and Lamond, A.I. (2010). Direct interaction between hnRNP-M and CDC5L/PLRG1 proteins affects alternative splice site choice. EMBO Rep. *11*, 445–451. https://doi.org/10.1038/embor.2010.64.
18. Drissi, R., Dubois, M.L., Douziech, M., and Boisvert, F.M. (2015). Quantitative proteomics reveals dynamic interactions of the minichromosome maintenance complex (MCM) in the cellular response to etoposide induced DNA damage. Mol. Cell. Proteomics *14*, 2002–2013. https://doi.org/10.1074/mcp.M115.048991.
19. Li, C.G., Mahon, C., Sweeney, N.M., Verschueren, E., Kantamani, V., Li, D., Hennigs, J.K., Marciano, D.P., Diebold, I., Abu-Halawa, O., et al. (2019). PPARγ Interaction with UBR5/ATMIN promotes DNA repair to maintain endothelial homeostasis. Cell Rep. *26*, 1333–1343.e7. https://doi.org/10.1016/j.celrep.2019.01.013.
20. Herrmann, C., Avgousti, D.C., and Weitzman, M.D. (2017). Differential salt fractionation of nuclei to analyze chromatin-associated proteins from cultured mammalian cells. Bio. Protoc. *7*, e2175. https://doi.org/10.21769/bioprotoc.2175.
21. Abdrabou, A., Brandwein, D., and Wang, Z. (2020). Differential subcellular distribution and translocation of seven 14-3-3 isoforms in response to EGF and during the cell cycle. Int. J. Mol. Sci. *21*, 318–324. https://doi.org/10.3390/ijms21010318.
22. Alanko, J., Mai, A., Jacquemet, G., Schauer, K., Kaukonen, R., Saari, M., Goud, B., and Ivaska, J. (2015). Integrin endosomal signalling suppresses anoikis. Nat. Cell Biol. *17*, 1412–1421. https://doi.org/10.1038/ncb3250.
23. Bolton, S.J., Barry, S.T., Mosley, H., Patel, B., Jockusch, B.M., Wilkinson, J.M., and Critchley, D.R. (1997). Monoclonal antibodies recognizing the N- and C-terminal regions of talin disrupt actin stress fibers when microinjected into human fibroblasts. Cell Motil Cytoskeleton *36*, 363–376. https://doi.org/10.1002/(SICI)1097-0169(1997)36:4<363::AID-CM6>3.0.CO;2-6.
24. Praekelt, U., Kopp, P.M., Rehm, K., Linder, S., Bate, N., Patel, B., Debrand, E., Manso, A.M., Ross, R.S., Conti, F., et al. (2012). New isoform-specific monoclonal antibodies reveal different sub-cellular localisations for talin1 and talin2. Eur. J. Cell Biol. *91*, 180–191. https://doi.org/10.1016/j.ejcb.2011.12.003.
25. Wang, P., Ballestrem, C., and Streuli, C.H. (2011). The C terminus of talin links integrins to cell cycle progression. J. Cell Biol. *195*, 499–513. https://doi.org/10.1083/jcb.201104128.
26. Robinson, M.D., McCarthy, D.J., and Smyth, G.K. (2010). edgeR: A Bioconductor package for differential expression analysis of digital gene expression data. Bioinformatics *26*, 139–140. https://doi.org/10.1093/bioinformatics/btp616.
27. Serrels, B., McGivern, N., Canel, M., Byron, A., Johnson, S.C., McSorley, H.J., Quinn, N., Taggart, D., Von Kreigsheim, A., Anderton, S.M., et al. (2017). IL-33 and ST2 mediate FAK-dependent antitumor immune evasion through transcriptional networks. Sci. Signal. *10*, eaan8355. https://doi.org/10.1126/scisignal.aan8355.
28. Wang, Y., and Gilmore, T.D. (2003). Zyxin and paxillin proteins: Focal adhesion plaque LIM domain proteins go nuclear. Biochim. Biophys. Acta *1593*, 115–120. https://doi.org/10.1016/S0167-4889(02)00349-X.
29. Lim, S.-T., Chen, X.L., Lim, Y., Hanson, D.A., Vo, T.-T., Howerton, K., Larocque, N., Fisher, S.J., Schlaepfer, D.D., and Ilic, D. (2008). Nuclear FAK promotes cell proliferation and survival through FERM-enhanced p53 degradation. Mol. Cell *29*, 9–22. https://doi.org/10.1016/j.molcel.2007.11.031.
30. Frame, M.C., Patel, H., Serrels, B., Lietha, D., and Eck, M.J. (2010). The FERM domain: Organizing the structure and function of FAK. Nat. Rev. Mol. Cell Biol. *11*, 802–814. https://doi.org/10.1038/nrm2996.
31. Griffith, B.G.C., Upstill-Goddard, R., Brunton, H., Grimes, G.R., Biankin, A.V., Serrels, B., Byron, A., and Frame, M.C. (2021). FAK regulates IL-33 expression by controlling chromatin accessibility at c-Jun motifs. Sci. Rep. *11*, 229. https://doi.org/10.1038/s41598-020-80111-9.

32. Klages-Mundt, N.L., Kumar, A., Zhang, Y., Kapoor, P., and Shen, X. (2018). The nature of actin-family proteins in chromatin-modifying complexes. Front. Genet. *9*, 398. https://doi.org/10.3389/fgene.2018.00398.
33. Almuzzaini, B., Sarshad, A.A., Farrants, A.K.Ö., and Percipalle, P. (2015). Nuclear myosin 1 contributes to a chromatin landscape compatible with RNA polymerase II transcription activation. BMC Biol. *13*, 35. https://doi.org/10.1186/s12915-015-0147-z.
34. Xu, X., Hua, X., Brown, K., Ren, X., and Zhang, Z. (2022). Mcm2 promotes stem cell differentiation via its ability to bind H3-H4. Elife *11*, e80917. https://doi.org/10.7554/eLife.80917.
35. Joutsen, J., Da Silva, A.J., Luoto, J.C., Budzynski, M.A., Nylund, A.S., de Thonel, A., Concordet, J.P., Mezger, V., Sabéran-Djoneidi, D., Henriksson, E., and Sistonen, L. (2020). Heat shock factor 2 protects against proteotoxicity by maintaining cell-cell adhesion. Cell Rep. *30*, 583–597.e6. https://doi.org/10.1016/j.celrep.2019.12.037.
36. Da Silva, A.J., Hästbacka, H.S.E., Luoto, J.C., Gough, R.E., Coelho-Rato, L.S., Laitala, L.M., Goult, B.T., Imanishi, S.Y., Sistonen, L., and Henriksson, E. (2024). Proteomic profiling identifies a direct interaction between heat shock transcription factor 2 and the focal adhesion adapter talin-1. FEBS J. *291*, 4830–4848. https://doi.org/10.1111/febs.17271.
37. Dongre, A., and Weinberg, R.A. (2019). New insights into the mechanisms of epithelial–mesenchymal transition and implications for cancer. Nat. Rev. Mol. Cell Biol. *20*, 69–84. https://doi.org/10.1038/s41580-018-0080-4.
38. Janota, C.S., Calero-Cuenca, F.J., and Gomes, E.R. (2020). The role of the cell nucleus in mechanotransduction. Curr. Opin. Cell Biol. *63*, 204–211. https://doi.org/10.1016/j.ceb.2020.03.001.
39. Jahed, Z., and Mofrad, M.R. (2019). The nucleus feels the force, LINCed in or not. Curr. Opin. Cell Biol. *58*, 114–119. https://doi.org/10.1016/j.ceb.2019.02.012.
40. Miroshnikova, Y.A., Cohen, I., Ezhkova, E., and Wickström, S.A. (2019). Epigenetic gene regulation, chromatin structure, and force-induced chromatin remodelling in epidermal development and homeostasis. Curr. Opin. Genet. Dev. *55*, 46–51. https://doi.org/10.1016/j.gde.2019.04.014.
41. Khilan, A.A., Al-Maslamani, N.A., and Horn, H.F. (2021). Cell stretchers and the LINC complex in mechanotransduction. Arch. Biochem. Biophys. *702*, 108829. https://doi.org/10.1016/j.abb.2021.108829.
42. Perez-Riverol, Y., Bai, J., Bandla, C., García-Seisdedos, D., Hewapathirana, S., Kamatchinathan, S., Kundu, D.J., Prakash, A., Frericks-Zipper, A., Eisenacher, M., et al. (2022). The PRIDE database resources in 2022: A hub for mass spectrometry-based proteomics evidences. Nucleic Acids Res. *50*, D543–D552. https://doi.org/10.1093/nar/gkab1038.
43. Ge, S.X., Jung, D., Yao, R., and Yao, R. (2020). ShinyGO: A graphical gene-set enrichment tool for animals and plants. Bioinformatics *36*, 2628–2629. https://doi.org/10.1093/bioinformatics/btz931.
44. Schindelin, J., Arganda-Carreras, I., Frise, E., Kaynig, V., Longair, M., Pietzsch, T., Preibisch, S., Rueden, C., Saalfeld, S., Schmid, B., et al. (2012). Fiji: An open-source platform for biological-image analysis. Nat. Methods *9*, 676–682. https://doi.org/10.1038/nmeth.2019.
45. Legland, D., Arganda-Carreras, I., and Andrey, P. (2016). MorphoLibJ: Integrated library and plugins for mathematical morphology with ImageJ. Bioinformatics *32*, 3532–3534. https://doi.org/10.1093/bioinformatics/btw413.
46. Ollion, J., Cochennec, J., Loll, F., Escudé, C., and Boudier, T. (2013). TANGO: A generic tool for high-throughput 3D image analysis for studying nuclear organization. Bioinformatics *29*, 1840–1841. https://doi.org/10.1093/bioinformatics/btt276.
47. Brocher, J. (2023). biovoxxel/BioVoxxel-Toolbox: BioVoxxel Toolbox v2.6.0 (Zenodo). https://doi.org/10.5281/zenodo.8214743.
48. Stirling, D.R., Swain-Bowden, M.J., Lucas, A.M., Carpenter, A.E., Cimini, B.A., and Goodman, A. (2021). CellProfiler 4: improvements in speed, utility and usability. BMC Bioinf. *22*, 433. https://doi.org/10.1186/s12859-021-04344-9.
49. Dobin, A., Davis, C.A., Schlesinger, F., Drenkow, J., Zaleski, C., Jha, S., Batut, P., Chaisson, M., and Gingeras, T.R. (2013). STAR: Ultrafast universal RNA-seq aligner. Bioinformatics *29*, 15–21. https://doi.org/10.1093/bioinformatics/bts635.
50. Liao, Y., Smyth, G.K., and Shi, W. (2014). FeatureCounts: An efficient general purpose program for assigning sequence reads to genomic features. Bioinformatics *30*, 923–930. https://doi.org/10.1093/bioinformatics/btt656.
51. Su, S., Law, C.W., Ah-Cann, C., Asselin-Labat, M.L., Blewitt, M.E., and Ritchie, M.E. (2017). Glimma: Interactive graphics for gene expression analysis. Bioinformatics *33*, 2050–2052. https://doi.org/10.1093/bioinformatics/btx094.
52. Dang, C.V., and Lee, W.M. (1988). Identification of the human c-myc protein nuclear translocation signal. Mol. Cell Biol. *8*, 4048–4054. https://doi.org/10.1128/mcb.8.10.4048-4054.1988.
53. Rueden, C.T., Schindelin, J., Hiner, M.C., DeZonia, B.E., Walter, A.E., Arena, E.T., and Eliceiri, K.W. (2017). ImageJ2: ImageJ for the next generation of scientific image data. BMC Bioinf. *18*, 529. https://doi.org/10.1186/s12859-017-1934-z.

STAR★METHODS

KEY RESOURCES TABLE

REAGENT or RESOURCE	SOURCE	IDENTIFIER
Antibodies		
Monoclonal Anti-α-Tubulin (mouse)	DSHB	Cat#12G10; RRID:AB_2315509
Monoclonal Anti-β-Tubulin (mouse)	Sigma-Aldrich	Cat#T8328; RRID:AB_1844090
Anti-β1 Integrin (mouse)	BD Biosciences	Cat#610468; RRID:AB_397840
Monoclonal Anti-Histone H4 (rabbit)	Millipore	Cat#05–858; RRID:AB_390138
Monoclonal Anti-HSC70 (rat)	Ezo Life Sciences	Cat#ADI-SPA-815; RRID:AB_10617277
Polyclonal Anti-Lamin A/C (rabbit)	Abcam	Cat#ab26300; RRID:AB_775965
Monoclonal Anti-TLN1 205 (mouse)	Abcam	Cat#ab78291; RRID:AB_2204000
Monoclonal Anti-TLN1 8D4 (mouse)	Sigma Aldrich	Cat#T3287; RRID:AB_477572
Monoclonal Anti-TLN1 93E12 (mouse)	Abcam	Cat#ab104913; RRID:AB_10858284
Monoclonal Anti-MCM2 EPR4120 (rabbit)	Abcam	Cat#ab108935; RRID:AB_10859977
Monoclonal Anti-GFP mouse (mouse)	Abcam	Cat#ab1218; RRID:AB_298911
Polyclonal Anti-GFP rabbit (rabbit)	Thermo Scientific	Cat#A-11122; RRID:AB_221569
Monoclonal Anti-FAK B-8 (mouse)	Santa Cruz Biotechnology	Cat#sc-271195; RRID:AB_10610506
Monoclonal Anti-FAK (phospho Y397) [EP2160Y]	Abcam	Cat#ab81298; RRID:AB_1640500
Anti-mouse IgG, HRP-linked antibody	Promega	Cat#W4021; RRID:AB_430834
Anti-rabbit IgG, HRP-linked antibody	Promega	Cat#W4011; RRID:AB_430833
Anti-rat IgG, HRP-linked antibody	GE Healthcare	Cat#NA935V; RRID: AB_772207
Goat anti-rabbit Alexa Fluor 546	Life Technologies	Cat#A11010; RRID: AB_2534077
Goat anti-mouse Alexa Fluor 488	Life Technologies	Cat#A11001; RRID: AB_2534069
Chemicals, peptides, and recombinant proteins		
Cholera toxin	Sigma-Aldrich	Cat#C8052
Fetal Bovine Serum	Serana	Cat#S-FBS-SA-015
VECTASHIELD	Vector Laboratories	Cat#H-1000
Enhanced Chemiluminescence Reagent	GE Healthcare	Cat#28980926
Enhanced Chemiluminescence Reagent Pico	Thermo Fisher Scientific	Cat#34579
Enhanced Chemiluminescence Reagent Femto	Thermo Fisher Scientific	Cat#34094
DMEM/F12	Gibco	Cat#11330-032
DMEM	Sigma-Aldrich	Cat#D6171
RPMI	Sigma-Aldrich	Cat#1640
Trypsin-EDTA	Gibco	Cat#25200058
Horse serum	Gibco	Cat#26050-070
Insulin	Gibco	Cat#A11382II
EGF	Gibco	Cat#AF-100-15-1MG
Hydrocortisone	Sigma-Aldrich	Cat#H0888
Protease inhibitor cocktail	Roche Diagnostics	Cat#04693159001
Micrococcal nuclease	New England Biolabs	Cat#M02475
Critical commercial assays		
Duolink® Blocking Solution	Merck	Cat#DUO82007
Duolink® Antibody Diluent	Merck	Cat#DUO82008
Duolink® Probe Anti-Rabbit Plus	Merck	Cat#DUO92002
Duolink® Probe Anti-Mouse Minus	Merck	Cat#DUO92004
Duolink® *In situ* Detection Reagent	Merck	Cat#DUO92008
Duolink® *In Situ* Mounting Media	Merck	Cat#DUO82040

(*Continued on next page*)

Continued

REAGENT or RESOURCE	SOURCE	IDENTIFIER
RNeasy plus mini kit	QIAGEN	Cat#74136
NE-PER Nuclear and Cytoplasmic Extraction Reagents	Thermo Fisher Scientific	Cat#78833
RNeasy mini kit	QIAGEN	Cat#74106
RNeasy plus mini kit	QIAGEN	Cat#74136
AllPrep DNA/RNA/miRNA universal kit	QIAGEN	Cat#80224
PowerUP SYBR green master mix	Thermo Fisher Scientific	Cat#MAN0028468
In-Fusion HD cloning kit	Takara Bio	Cat#639650
iScript cDNA Synthesis Kit	Bio-Rad	Cat#1708891
Deposited data		
RNA-seq data	This paper; Gene Expression Omnibus	GSE198191
Mass Spectrometry	This paper; ProteomeXchange	PXD058465
Experimental models: Cell lines		
MCF10A	ATCC	Cat#CRL-10317; RRID:CVCL_0598
MDA-MB-231	ATCC	Cat#HTB-26; RRID:CVCL_0062
HS578T	ATCC	Cat#HTB-126; RRID:CVCL_0332
PC3	ATCC	Cat#CRL-1435; RRID:CVCL_0035
Oligonucleotides		
siRNAs specific for TLN1	Dharmacon	Cat#J-012949-06-0010
siRNAs specific for TLN1	Dharmacon	Cat#J-012949-07-0010
ON-TARGETplus Non-targeting control pool	Dharmacon	Cat#D-001810-10-20
See Table S6 for oligonucleotides used in cloning	This paper	N/A
See Table S8 for qPCR primers	This paper	N/A
Recombinant DNA		
TLN1-NLS plasmid	This paper	N/A
pEGFP-N2-NLS	This paper	N/A
pEGFP-N2 vector	Clontech	Cat#6081-1
Software and algorithms		
ShinyGO v0.66	Ge et al.[43]	https://bioinformatics.sdstate.edu/go/; RRID:SCR_019213
Fiji	Schindelin et al.[44]	https://fiji.sc/; RRID:SCR_002285
MorphoLibJ v1.6.2	Legland et al.[45]	https://github.com/ijpb/MorphoLibJ
3DSuite plugin v4.1.5	Ollion et al.[46]	https://framagit.org/mcib3d/mcib3d-core
BioVoxxel Toolbox v2.6.0	Brocher et al.[47]	https://github.com/biovoxxel/BioVoxxel-Toolbox
CellProfiler v4.2.6	Stirling et al.[48]	https://cellprofiler.org; RRID:SCR_007358
FastQC v0.11.9	N/A	http://www.bioinformatics.babraham.ac.uk/projects/fastqc/; RRID:SCR_014583
STAR aligner v2.7.9a	Dobin et al.[49]	https://github.com/alexdobin/STAR; RRID:SCR_004463
Subread v2.0.1	Liao et al.[50]	https://subread.sourceforge.net/; RRID:SCR_009803
edgeR v3.34.1	Robinson et al.[26]	https://bioconductor.org/packages/release/bioc/html/edgeR.html; RRID:SCR_012802
Glimma v2.2.0	Su et al.[51]	https://bioconductor.org/packages/release/bioc/html/Glimma.html; RRID:SCR_017389

(*Continued on next page*)

Continued

REAGENT or RESOURCE	SOURCE	IDENTIFIER
pheatmap v1.0.12	N/A	https://CRAN.R-project.org/package = pheatmap; RRID:SCR_016418
Spectronaut 18.0.2	Biognosys	https://biognosys.com/software/spectronaut/
Thermo Xcalibur 4.6	Thermo Fisher Scientific	https://www.thermofisher.com/us/en/home/industrial/mass-spectrometry/liquid-chromatography-mass-spectrometry-lc-ms/lc-ms-software/lc-ms-data-acquisition-software/xcalibur-data-acquisition-interpretation-software.html
IBright Analysis Software 5.3.0	Thermo Fisher Scientific	https://www.thermofisher.com/us/en/home/technical-resources/software-downloads/ibright-western-imager.html; RRID:SCR_017632
GraphPad Prism 7	GraphPad	https://www.graphpad.com; RRID:SCR_002798
Other		
MatTek plates	MatTek corporation	Cat#P35GC-1.5-14-C
Ultra-Low Attachment (ULA) plates	Corning	Cat#7007
NEON Transfection System	Thermo Fisher Scientific	Cat#MPK5000

EXPERIMENTAL MODEL AND STUDY PARTICIPANT DETAILS

Cell lines

All cells were maintained at 37°C in a humidified 5% CO_2 atmosphere. MCF10A cells were cultured in DMEM/F12 (Dulbecco's Modified Eagle's Media/Nutrient Mixture F-12, 11330-032, Gibco) medium supplemented with 100 ng/mL cholera toxin, 5% horse serum, 10 μg/mL insulin, 20 ng/mL EGF, 0.5 ng/mL hydrocortisone, and 100 μg/mL penicillin-streptomycin. HS578T cells were cultured in DMEM (D6171, Sigma-Aldrich) supplemented with 10% fetal bovine serum, 2 mM L-glutamine, 100 μg/mL penicillin-streptomycin, and 10 μg/mL insulin. MDA-MB-231 and U2OS cells were cultured in DMEM (D6171, Sigma-Aldrich) supplemented with 10% fetal bovine serum, 2 mM L-glutamine, and 100 μg/mL penicillin-streptomycin. PC3 cells were cultured in RPMI (Roswell Park Memorial Institute, 1640, Sigma-Aldrich) supplemented with 10% fetal bovine serum, 2 mM L-glutamine, and 100 μg/mL penicillin-streptomycin. All cell lines were cultured at 37°C and routinely tested for mycoplasma. The cells were authenticated by ATCC as the commercial supplier. Detailed information regarding the cell lines used is provided in the key resources table.

METHOD DETAILS

Transfections and gene silencing

All transfections were performed using the NEON Transfection System (MPK5000, Thermo Fisher Scientific) according to the manufacturer's instructions. Briefly, 2.2×10^6 HS578T cells were suspended in 100 μL of resuspension buffer, mixed with either 13 μg of DNA or 1.6 μM of RNA, and electroporated using 3 × 20 ms 1050 V pulses. To silence TLN1 an equal mixture (1:1) of two siRNAs was used, the siRNAs were purchased from Dharmacon: J-012949-06-0010 and J-012949-07-0010. As a control the ON-TARGETplus Non-targeting control pool from Dharmacon was used (D-001810-10-20). RNAs were utilized either at a final concentration of 1.6 μM for 48 h (for RNA-seq samples) or at a final concentration of 2.4 μM for 96 h (for immunofluorescence samples).

Plasmid construction

The TLN1-NLS plasmid was generated by cloning full-length human TLN1 from PC3 cells. Total RNA was isolated with RNeasy mini kit (74106, QIAGEN) and the complementary DNA was synthetized using random hexamer primers (SO142, Thermo Fisher Scientific). The full-length TLN1 was inserted into a pEGFP-N2 vector using the In-Fusion HD cloning kit (Takara Bio). Silent mutations on TLN1 were generated with the QuikChange II site-directed mutagenesis kit (Agilent Technologies) to make our construct resistant against the previously described siRNA specific for TLN1 (J-012949-06-0010 and J-012949-07-0010, Dharmacon). Finally, a double-stranded DNA fragment containing a Strep-tag II and the NLS of c-myc[52] was purchased from Eurofins Genomics and inserted in the C-termini of GFP with the In-Fusion HD cloning kit (Takara Bio). The EGFP-NLS plasmid was generated by deletion of TLN1 from the TLN1-NLS plasmid using the In-Fusion HD cloning kit (Takara Bio). All primers used for the plasmid construction are listed in Table S6.

Gene ontology (GO) term analysis

GO term analyses were performed with the online application ShinyGO.[43] For analysis performed with ShinyGO v.0.66 the following parameters were used: species: human, p-value cutoff: 0.05, and number of top pathways to show: 30.

Subcellular fractionations

Cells (MCF10A, MDA-MB-231, HS578T, and PC3) were treated with trypsin, collected in culture media, washed with PBS, and counted. Of the cell suspension, 13% was set apart for preparation of the whole cell lysate using lysis buffer (10% glycerol, 1 mM EDTA pH 7.4, 150 mM NaCl, 2 mM $MgCl_2$, 1% Triton X-100, 50 mM HEPES pH 7.4, Protease Inhibitor Cocktail [04693159001, Roche Diagnostics], 50 mM NaF, 0.2 mM Na_3VO_4). The remaining (87%) cell suspension was used for subcellular fractionation. Cytoplasmic, nuclear, and chromatin fractions were prepared using NE-PER Nuclear and Cytoplasmic Extraction Reagents (78833, Thermo Fisher Scientific) according to manufacturer's instructions. Briefly, the wet volume of the cell pellet was estimated by considering that 2×10^6 cells is equal to 20 μL of wet volume. The cell pellet was suspended in cytoplasmic extraction reagent I (CER I), vortexed for 15 s, and incubated on ice (see Table S7 for incubation and vortex times per cell line). After incubation, the cytoplasmic extraction reagent II (CER II) was added. The suspension was incubated on ice and centrifuged (20,000 × g, 5 min). The supernatant was collected (cytoplasmic fraction), and the pellet was washed three times with cold PBS. After washes, the pellet was resuspended in 100 μL of nuclear extraction reagent (NER), incubated on ice and centrifuged (20,000 × g, 10 min). The supernatant (nuclear fraction) was collected, and the pellet was washed three times with cold PBS. Following the washes with PBS, the pellet was resuspended in nuclear extraction reagent, supplemented with 1×10^3 micrococcal nuclease (M02475, New England Biolabs), 5 mM $CaCl_2$, and Protease Inhibitor Cocktail (04693159001, Roche Diagnostics), and incubated at 37°C for 5 min. After incubation the suspension was centrifuged (20,000 × g, 10 min) and the supernatant was stored as the chromatin fraction. The protein concentrations of the fractions were determined by BCA assay (23225, Thermo Fischer Scientific).

Differential salt fractionation

Once the nuclear fraction was collected, the pellet was incubated for 30 min at room temperature with the corresponding dilution of NaCl. NaCl was diluted in water and the following concentrations were used: 0.3, 0.45, 0.6, 0.8, and 1.2 M. After incubation in the first fraction of the NaCl gradient, the suspension was centrifuged (20,000×g, 10 min), the supernatant was collected, and the pellet was incubated in the second fraction. This procedure was repeated consecutively until the pellet was exposed to all the concentrations of NaCl.

Immunoblotting

Cells were washed and collected in PBS (L0615, BioWest). After collection, the cells were lysed in lysis buffer (10% glycerol, 1 mM EDTA pH 7.4, 150 mM NaCl, 2 mM $MgCl_2$, 1% Triton X-100, 50 mM HEPES pH 7.4, Protease Inhibitor Cocktail [04693159001, Roche Diagnostics], 50 mM NaF, 0.2 mM Na_3VO_4). The protein concentration was determined by BCA assay (23225, Thermo Fischer Scientific). Equal amounts of total protein were resolved on 4–20% Mini-PROTEAN TGX precast gels (Bio-Rad). The proteins were transferred to a nitrocellulose membrane, which was blocked in 5% milk-PBS with 0.3% Tween 20 for 1 h at room temperature. Membranes used for blotting with anti-FAK antibodies were instead blocked in 2% BSA-PBS with 0.1% Tween 20. The anti-FAK antibodies were diluted in 0.5% BSA-TBS-0.2% NaN_3, and the other primary antibodies in 0.5% BSA-PBS-0.02% NaN_3. The following primary antibodies were used: anti-α Tubulin (AB 1157911, Developmental Studies Hybridoma Bank), anti-β Tubulin (T8328, Sigma-Aldrich), anti-β1 Integrin (610468, BD Biosciences), anti-FAK B-8 (sc-271195, Santa Cruz Biotechnology), anti-FAK (phospho Y397 (ab81298, abcam), anti-Histone H4 (05–858, Millipore), anti-HSC70 (ADI-SPA-815, Enzo Life Sciences), anti-Lamin A/C (ab26300, Abcam), anti-TLN1 205 (ab78291, Abcam), and anti-TLN1 8D4 (T3287, Sigma Aldrich). The nitrocellulose membranes were incubated with the primary antibodies overnight at 4°C. Secondary HRP-conjugated antibodies were purchased from Promega or GE Healthcare (anti-mouse W4021, Promega; anti-rabbit W4011, Promega; anti-rat NA935V, GE Healthcare). The secondary antibodies were diluted in 5% milk-PBS with 0.3% Tween 20, except for the anti-FAK blots, where dilutions in 2% BSA-PBS with 0.1% Tween 20 were used. The nitrocellulose membranes were incubated with the secondary antibodies at least 1 h at room temperature, and then incubated with enhanced chemiluminescence reagent (28980926, GE Healthcare; 34579, Thermo Fisher Scientific; 34094, Thermo Fisher Scientific). Images were acquired with an iBright imaging system (Thermo Fisher Scientific) or a curix 60 X-ray film processor (Agfa). Unless indicated, all immunoblotting experiments were performed three times. The iBright analysis software (Thermo Fisher Scientific) was used for quantification of immunoblots.

Immunofluorescence and confocal microscopy

For confocal microscopy analyses, 8×10^4 HS578T or MDA-MB-231 cells were plated on MatTek plates (P35GC-1.5-14-C MatTek corporation) 48 h before imaging. Cells were fixed with 4% paraformaldehyde for 10 min, washed three times with PBS, permeabilized with 0.5% Triton X-100 and 3 mM EDTA in PBS, and washed again three times with PBS. The cells were blocked with 10% FBS-PBS for at least 1 h at room temperature, incubated overnight at 4°C with primary antibodies diluted in 10% FBS-PBS 1:220 anti-Lamin A/C (ab26300, Abcam) and 1:100 anti-TLN1 205 (ab78291, Abcam), and washed three times with PBS. Thereafter the cells were incubated for 1 h at room temperature with secondary antibodies goat anti-rabbit Alexa Fluor 546 (A11010, Life Technologies) and goat anti-mouse Alexa Fluor 488 (A11001, Life Technologies) diluted 1:500 in 10% FBS-PBS, washed in PBS, and incubated with

300 nM DAPI diluted in PBS for 5 min. The cells were washed with PBS and covered with VECTASHIELD (H-1000, Vector Laboratories) mounting medium. Images were captured with a 3i CSU-W1 spinning disc confocal microscope (Intelligent Imaging Innovations).

The voxel intensity in the immunofluorescence staining was quantified using Fiji (ImageJ, version: 1.54f).[44] To make a nuclear mask, the signal in the z stack corresponding to the DAPI channel was processed using the Median Filter (radius 20) and segmented using Yen thresholding. The binary images were subjected to Fill Holes and Analyze Particles (Size(pixelˆ2):0–100; circularity: Default; Show: masks). Subsequently, the Connecting Components Labeling plugin (MorphoLibJ v1.6.2)[45] was used with the following parameters: Connectivity: 26; Type of result: 8 bits. After constructing the nuclear mask, a composite of the mask and the z stack corresponding to the TLN1 immunostaining was generated. Finally, the Quantif 3D option of the 3D Manager within the 3DSuite plugin (v 4.1.5)[46] was used to quantify the sum of voxel intensity in the nuclear area within the corresponding z stack. Nuclei that were in contact with each other or with the borders of the image were excluded, and at least 90 cells were analyzed in each treatment (Scr vs. siTLN1).

Proximity ligation assay (PLA)

Proximity ligation assay (PLA) by Duolink was performed according to the manufacturer's recommendation with a few modifications. In brief, U2OS cells were seeded on 13 mm cover slips and with a confluency of 60%–70%, fixed with 4% paraformaldehyde for 10 min at room temperature followed by permeabilization with 0.5% Triton X-100, 3 mM EDTA in PBS for 30 min. The coverslips were washed three times with PBS for 10 min on a shaker, whereafter the cells were either stored at 4°C until further use. The coverslips were blocked using 40 μL of the Duolink Blocking Solution (DUO82007, Merck) in a heated humidity chamber for 60 min at 37°C. The coverslips were then incubated overnight at 4°C with 1 μg of the primary antibodies anti-TLN1 [93E12] (ab104913, Abcam), anti-MCM2 [EPR4120] (ab108935, Abcam) anti-GFP mouse (ab1218, Abcam), and anti-GFP rabbit (A-11122, Thermo Scientific), diluted in 100 μL of Duolink Antibody Diluent (DUO82008, Merck). The probes (DUO92002, DUO92004, Merck), ligation, and amplification (DUO92008, Merck) reactions were performed according to the manufacturer's recommendations. The samples were mounted in Duolink *In Situ* Mounting Media with DAPI (DUO82040, Merck) and kept in darkness until imaging with a 3i CSU-W1 spinning disk confocal microscope (Intelligent Imaging Innovations) using a 20× objective and a step size of 0.63 μm. At least five stacked images were taken per PLA antibody pair in each biological replica.

The PLA confocal images were pre-processed, segmented, and analyzed using Fiji (ImageJ, version: 1.54f)[53] and CellProfiler software (v 4.2.6)[48] to quantify the PLA signal per cell. In brief, Fiji was employed to subtract background (rolling ball radius 50 pixels for the images with DAPI stain, and 5 for images with PLA signal) of images from a single focal plane. Subsequently, CellProfiler was utilized for segmentation, using OTSU thresholding to count PLA signals, with the DAPI stain serving as a mask for identifying nuclear localization.

Mass spectrometry

HS578T, MDA-MB-231, MCF10A, and PC3 cells were lysed in 6 M urea in 50 mM Tris-HCl, pH 8.0, reduced with 10 mM D,L-dithiothreitol, and alkylated with 40 mM iodoacetamide and digested overnight with sequencing grade modified trypsin (Promega). After digestion, peptide samples were desalted with a Sep-Pak tC18 96-well plate (Waters) and evaporated to dryness. Samples were dissolved in 0.1% formic acid and peptide concentration was determined with a NanoDrop device. For data-independent acquisition (DIA) analysis, 800 ng of peptides were injected and analyzed. Wash runs were submitted between each sample to reduce potential carry-over of peptides.

The LC-ESI-MS/MS analysis was performed on a nanoflow HPLC system (Easy-nLC1200, Thermo Fisher Scientific) coupled to the Q Exactive HF mass spectrometer (Thermo Fisher Scientific) equipped with a nano-electrospray ionization source. Peptides were first loaded on a trapping column and subsequently separated inline on a 15 cm C18 column (75 μm × 15 cm, ReproSil-Pur 3 μm 120 Å C18-AQ, Dr. Maisch HPLC GmbH). The mobile phase consisted of water with 0.1% formic acid (solvent A) or acetonitrile/water (80:20 (v/v) with 0.1% formic acid (solvent B). A 120-min gradient was used to elute peptides (62 min from 3% to 21% solvent B, followed by 48 min from 21% to 36% solvent B and in 5 min from 36% to 100% of solvent B, followed by 5 min wash stage with solvent B).

Samples were analyzed with a DIA LC-MS/MS method. MS data was acquired automatically by using Thermo Xcalibur 4.6 software (Thermo Fisher Scientific). In a DIA method a duty cycle contained one full scan (400–1000 m/z) and 40 DIA MS/MS scans covering the mass range 400–1000 with variable width isolation windows. Data analysis consisted of protein identifications and label free quantifications of protein abundances. Data was analyzed by Spectronaut software (Biognosys; version 18.0.2). DirectDIA approach was used to identify proteins and label-free quantifications were performed with MaxLFQ.

RNA-sequencing

HS578T cells were transfected with either Scr or a combination of two siRNAs specific for TLN1 (J-012949-06-0010 and J-012949-07-0010, Dharmacon). After 48 h the cells were collected, and total RNA was purified with AllPrep DNA/RNA/miRNA Universal Kit (80224, QIAGEN) according to manufacturer's instructions. The RNA library was prepared according to Illumina stranded RNA preparation guide (1000000124518). Briefly, poly-A containing RNA molecules were purified with poly-T oligo magnetic beads and fragmented with divalent cations under elevated temperatures. For first-strand cDNA synthesis, RNA fragments were copied using reverse transcriptase and random primers. In a second-strand cDNA synthesis, dUTP replaces dTTP to achieve strand specificity. Unique dual indexing adapters were ligated to each sample. The quality and concentration of cDNA samples were analyzed with Advanced Analytical Fragment Analyzer and Bioanalyzer 2100 (Agilent) and Qubit Fluorometric Quantitation (Life Technologies) with the Qubit dsDNA Quantitation, High sensitivity (32851). Samples were sequenced with NovaSeq 6000 S1 v1.5 (Ilumina). All the experimental steps after the RNA extraction were conducted in the Finnish Functional Genomics Center, Turku, Finland. RNA-sequencing was performed from two independent sample series.

FastQC v0.11.9 was used to confirm the quality of the raw reads. The paired-end reads were aligned to the human genome (primary assembly GRCh38.p13, GENCODE) with STAR version 2.7.9a,[49] using the default settings. The number of read pairs mapped to each genomic feature in release 33 of the GENCODE annotation was determined by featureCounts from subread v2.0.1.[50] Only read pairs where both ends aligned were counted. Differential gene expression analysis was performed from two biological replicates using the Bioconductor R package edgeR v3.34.1. Weakly expressed genes were filtered using filterByExpr defaults, and samples were normalized using the trimmed mean of M-values (TMM) method. The threshold for differentially expressed genes was a false discovery rate (FDR) < 0.05 and a $\log_2$ fold change of at least ±0.5, since the magnitude of gene expression changes was expected to be moderate. The gene expression data was visualized as an MA-plot, produced by the Bioconductor R package Glimma v2.2.0.[51] The CRAN R package pheatmap v1.0.12 was used to produce the heatmap of *Z* score transformed log2CPM values.

Quantitative RT-PCR (qRT-PCR)

RNA was isolated using a RNeasy plus mini kit (74136, QIAGEN) according to the manufacturer's instructions. For each sample, 0.9 μg of RNA was reverse transcribed with an iScript cDNA Synthesis Kit (#1708891, Bio-Rad). The PowerUp SYBR Green Master Mix kit (MAN0028468, Thermo Fisher Scientific) was used for qRT-PCR that was performed with the QuantStudio 3 Real-Time PCR system (Applied Biosystems, Thermo Fisher Scientific). The mRNA expression levels were normalized against the respective GAPDH expression in each sample. All reactions were run in triplicates from samples derived from three biological replicates. See Table S8 for primers used in the amplification step.

Ultra-low attachment assay

HS578T cells transiently transfected with plasmids encoding GFP or TLN1-NLS were collected 48 h post-transfection. After counting, 2.7×10^3 cells were placed in each well of a 96-well Ultra-Low Attachment (ULA) plate (#7007, Corning) with a total volume of 200 μL of cell media. Cells were visualized with Zeiss Axio Vert. A1 microscope (NA 0.4) after 2 h using a 10× objective. All images were analyzed with Fiji (ImageJ, version: 1.53t) using the BioVoxxel Toolbox plugin v2.6.0.[47] Briefly, the images were converted from 16 bit to 8 bit, the background was subtracted using a rolling ball radius of 50 pixels. The perimeter of the spheroids was segmented with the thresholding algorithm of Fiji choosing the dark background option, and the extended particle analyzer option of the BioVoxxel Toolbox plugin was run with default settings using the pixel units and output in pixel options. After obtaining the number of pixels for the corresponding spheroid, the size in micrometers was calculated.

QUANTIFICATION AND STATISTICAL ANALYSIS

Statistical analyses were performed with GraphPad Prism 7 Software (GraphPad Software). Statistical significance was analyzed using unpaired or paired two-tailed student's t-tests, Mann-Whitney tests, or two-tailed Welch's t-tests. Data are represented as individual values or mean +SEM or +SD and statistical significance as; $^{*}p < 0.05$, $^{**}p < 0.01$, $^{***}p < 0.001$, and $^{****}p < 0.0001$, respectively. The details for the statistical analyses used in individual experiments are described in the corresponding figure legends.